

A Complete Catalogue of Dusty Supernova Remnants in the Galactic Plane

14 January 2020

**APPENDIX A: FIR CATALOGUE OF SNRS
WITH *HERSCHEL***

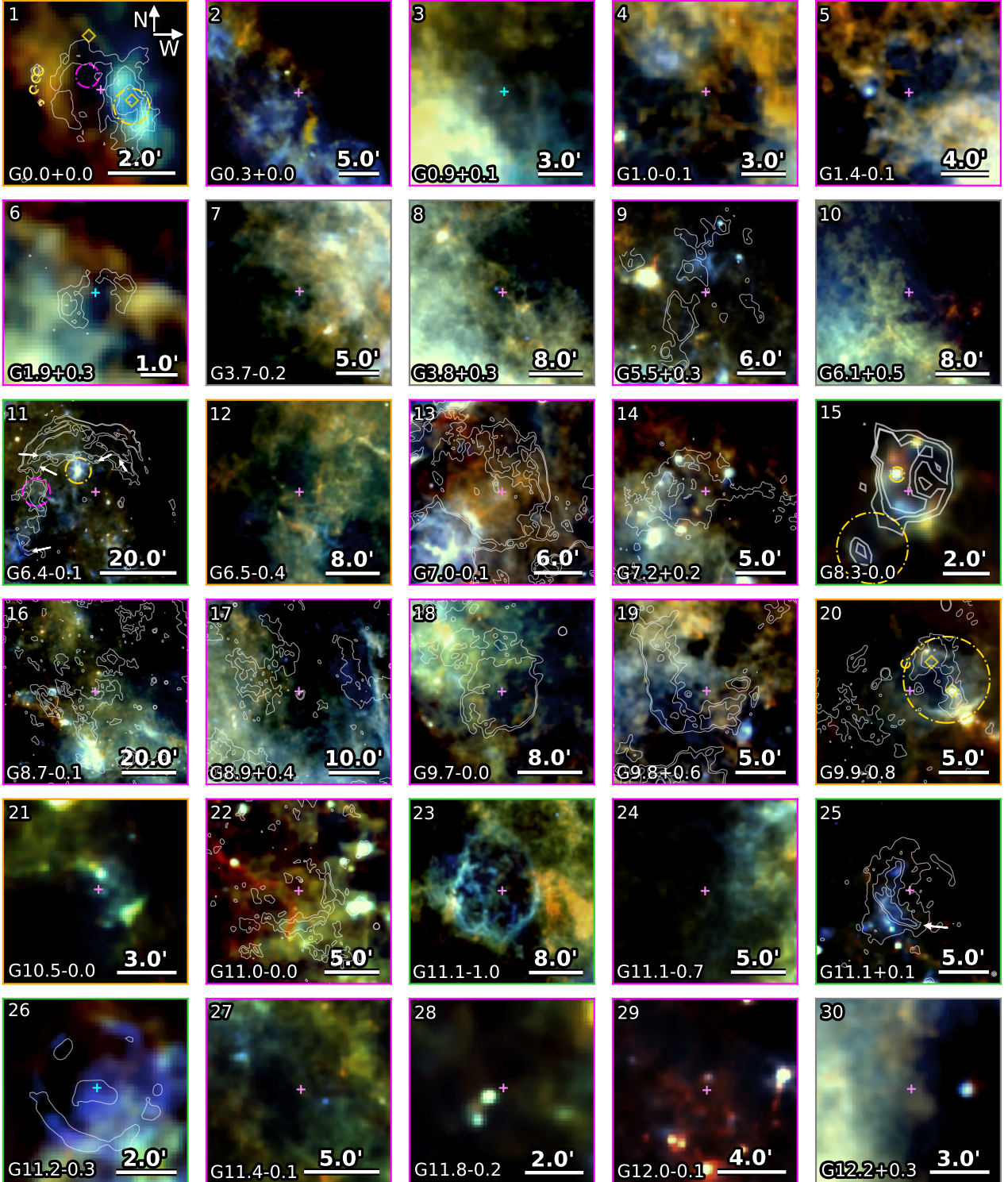


Figure A1. *Herschel* three colour images of the locations of all supernova remnants in our sample. Colours are red = $250\mu\text{m}$, green = $160\mu\text{m}$, and blue = $70\mu\text{m}$. Purple crosses indicate the source radio centre from Green (2014) and cyan crosses indicate the X-ray centre. The border colour indicates the associated detection level in this study, as given in Table A1, where green = level 1, orange = level 2, magenta = level 3, grey = level 4, and black = unstudied. In some panels dashed magenta circles and white arrows indicate particular FIR dust emission features associated with the SNR, gold circles indicate unrelated structure such as HII regions. Overlaid onto G0.0+0.0, the gold diamonds indicate the location of the associated neutron star and Sgr A*. The gold diamonds on the image of G9.9-0.8 indicate the locations of HII regions. VLA GPS 20 cm contours overlaid onto the images of G0.0+0.0, G7.0-0.1, G7.2+0.2, G8.3-0.0, G9.7-0.0, G9.8+0.6, and G11.0-0.0; *Chandra* contours are overlaid onto G1.9+0.3 and G11.2-0.3; 90 cm contours are overlaid onto G5.5+0.3, G6.4-0.1, G8.7-0.1, G8.9+0.4, and G9.9-0.8.

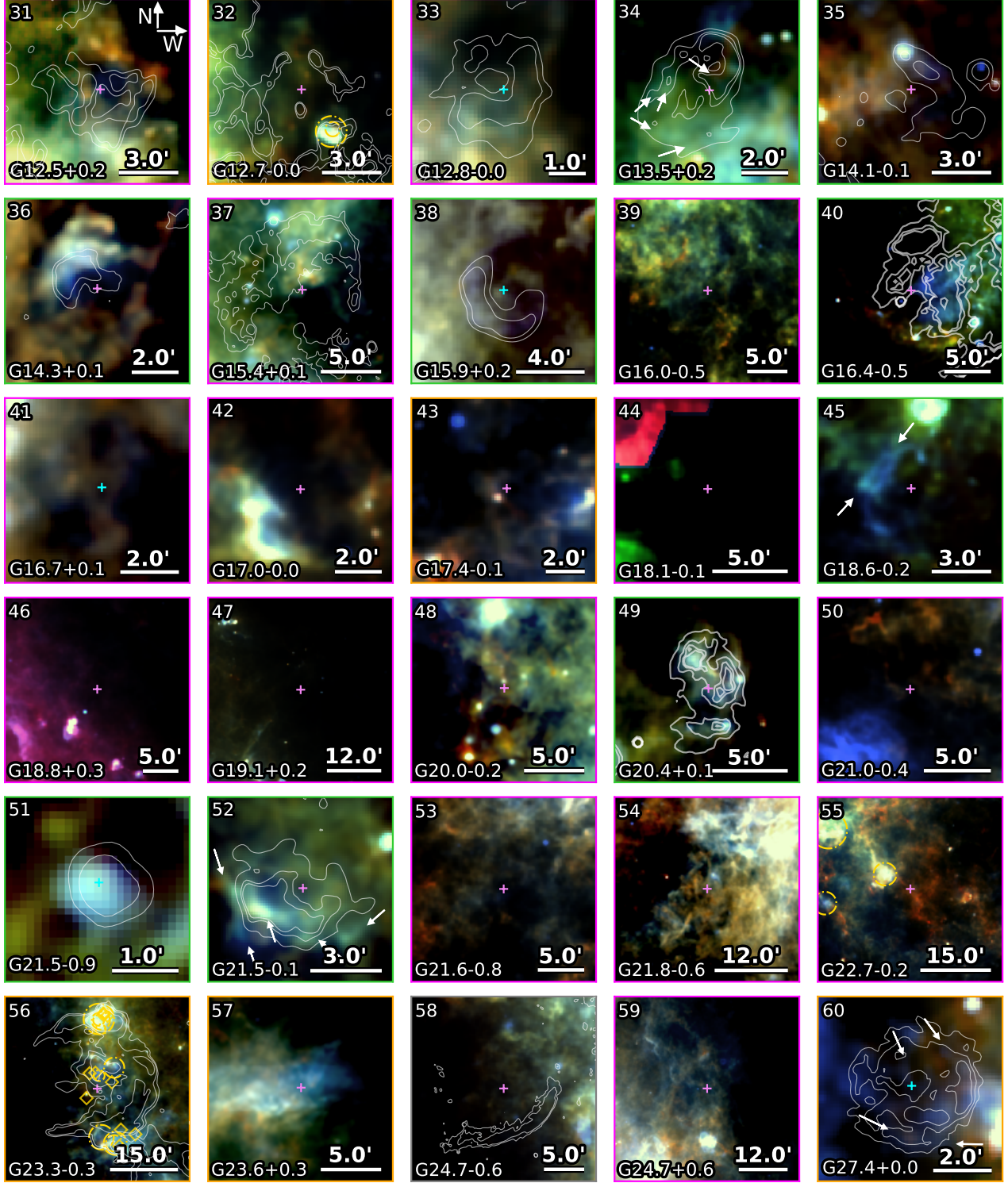


Figure A1 – continued VLA GPS 20 cm contours are overlaid onto G12.5+0.2, G12.7–0.0, G12.8–0.0, G13.5+0.2, G14.3+0.1, G20.4+0.1 and G24.7–0.6; VLA GPS 90 cm contours are overlaid onto G15.4+0.1; *Chandra* contours are overlaid onto G15.9+0.2, G21.5–0.9, and G27.4+0.0; MIPS 24 μ m contours are overlaid onto G14.1–0.1; VGPS 21 cm contours are overlaid onto G23.3–0.3. The gold diamonds overlaid onto the image of G23.2–0.3 indicate the locations of a gamma ray source (HESS J1834–087), OH (1720 MHz) maser lines, and other maser emission.

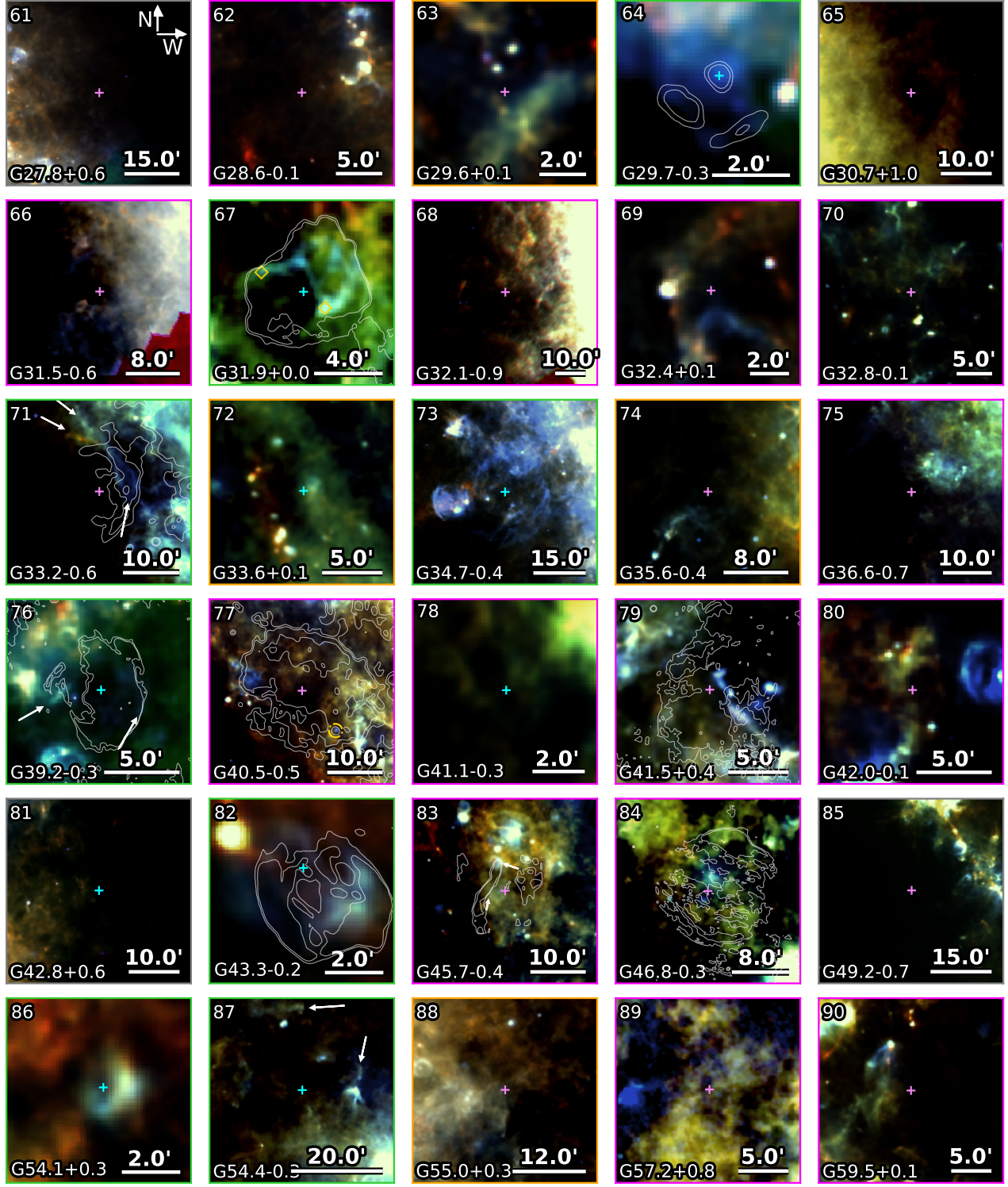


Figure A1 – continued *Chandra* contours are overlaid onto G29.7–0.3 and G33.6+0.1; VLA GPS 20 cm contours are overlaid onto G31.9+0.0, G33.2–0.6, G39.2–0.3, G41.5+0.4, G43.3–0.2, and G46.8–0.7; VGPS 21 cm contours are overlaid onto G40.5–0.5; NVSS 1.4 GHz contours are overlaid onto G45.7–0.4.

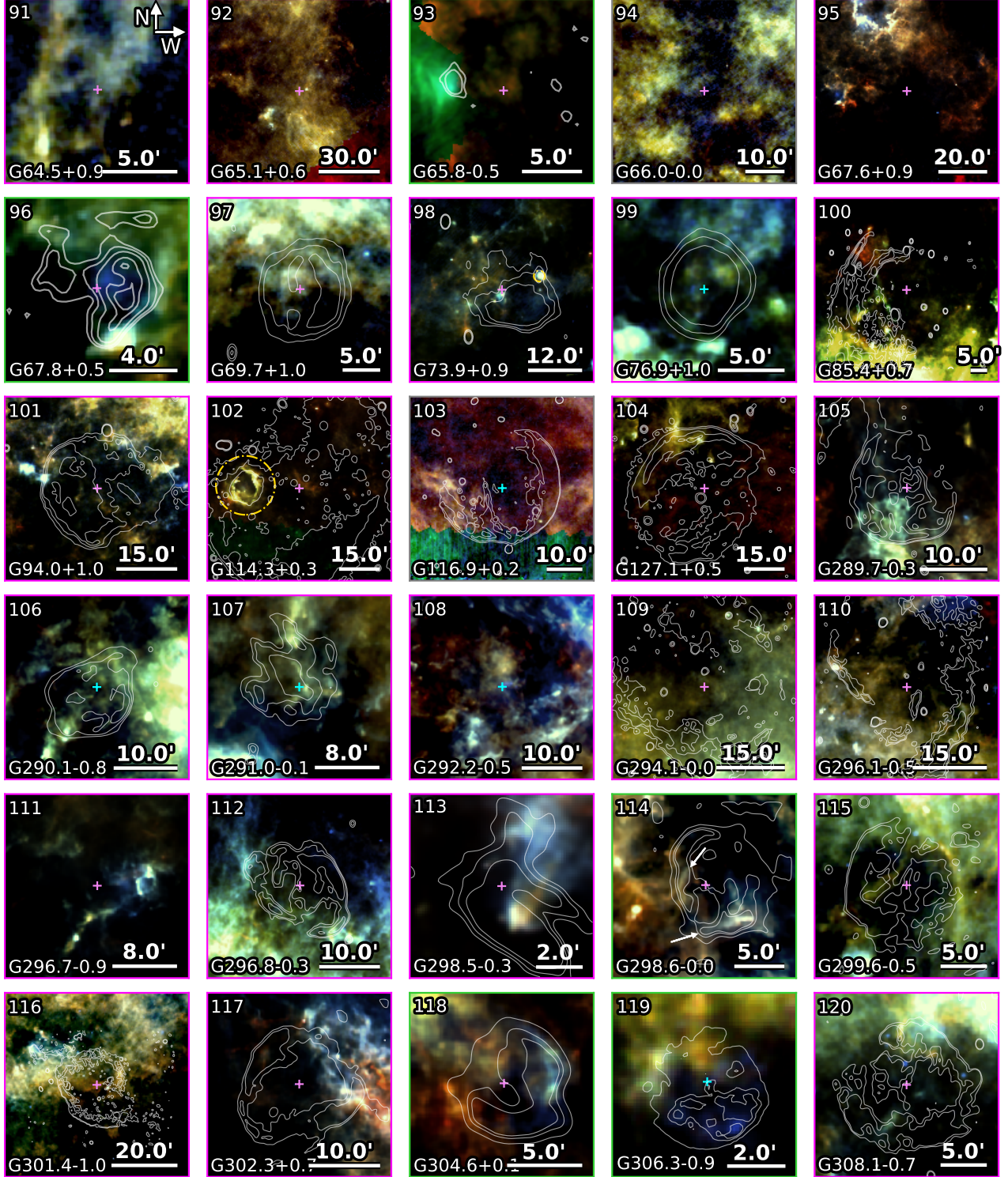


Figure A1 – continued NVSS 1.4 GHz contours are overlaid onto G65.8–0.5, and G67.8+0.5. Canadian Galactic Plane Survey (CGPS, 1420 MHz) contours are overlaid onto G69.7+1.0, G73.9+0.9, G76.9+1.0, G85.4+0.7, G94.0+1.0, G114.3+0.3, G116.9+0.2, and G127.1+0.5. MOST 843 MHz contours are overlaid onto G289.7–0.3, G290.1–0.8, G291.0–0.1, G294.1–0.0, G296.1–0.5, G296.8–0.3, G298.5–0.3, G298.6–0.0, G299.6–0.5, G301.4–1.0, G302.3+0.7, G304.6+0.1, and G308.1–0.7; *Chandra* contours are overlaid onto G306.3–0.9.

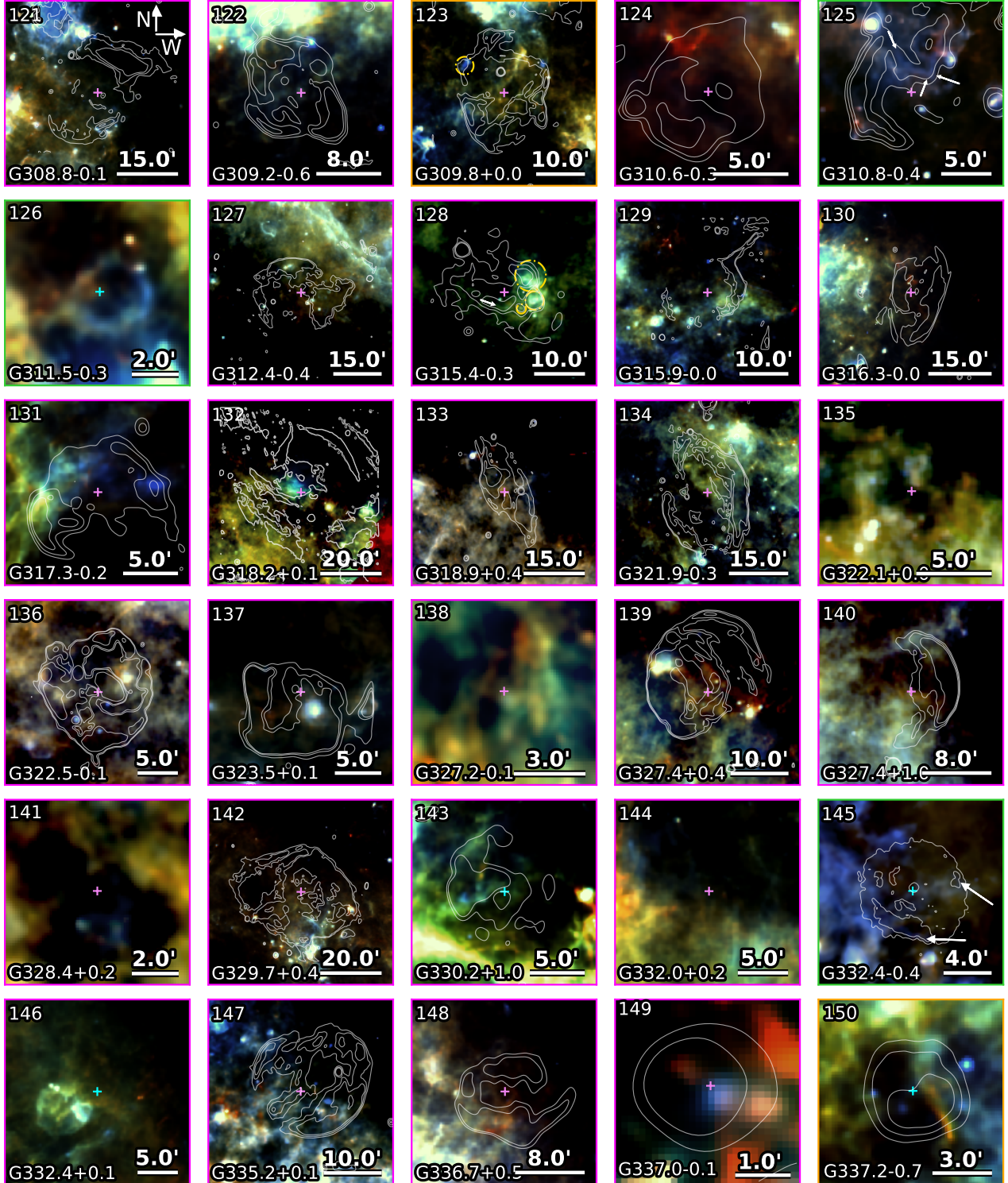


Figure A1 – continued *Chandra* contours are overlaid onto G332.4–0.4, all other contours are MOST 843 MHz .

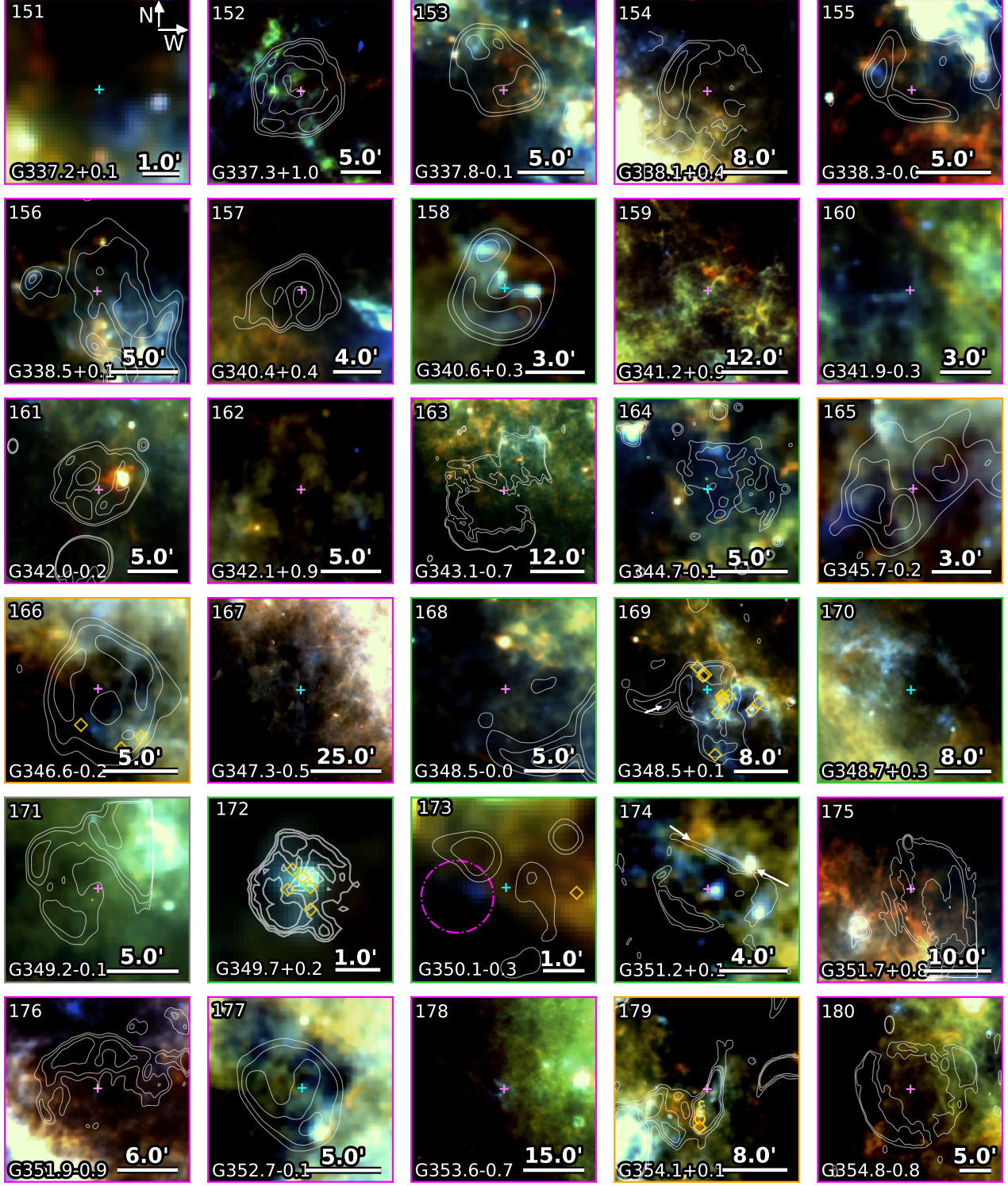


Figure A1 – continued MOST 843 MHz contours are overlaid onto G337.2–0.7, G342.2–0.2, G343.1–0.7, G345.7–0.2, G346.6–0.2, G348.5–0.0, G348.5+0.1, G349.2–0.1, G351.2+0.1, G351.7+0.8, G351.9–0.9, G352.7–0.1, G3541+0.1, and G354.8–0.8; MIPS 24 μ m contours are overlaid onto G344.7–0.1 and G350.1–0.3; Chandra contours are overlaid onto G349.7+0.2. The diamonds overlaid onto the images of G350.1–0.3 and G354.1+0.1 indicate the locations of an associated neutron star and pulsar respectively. All other diamonds indicate the locations of maser emission.

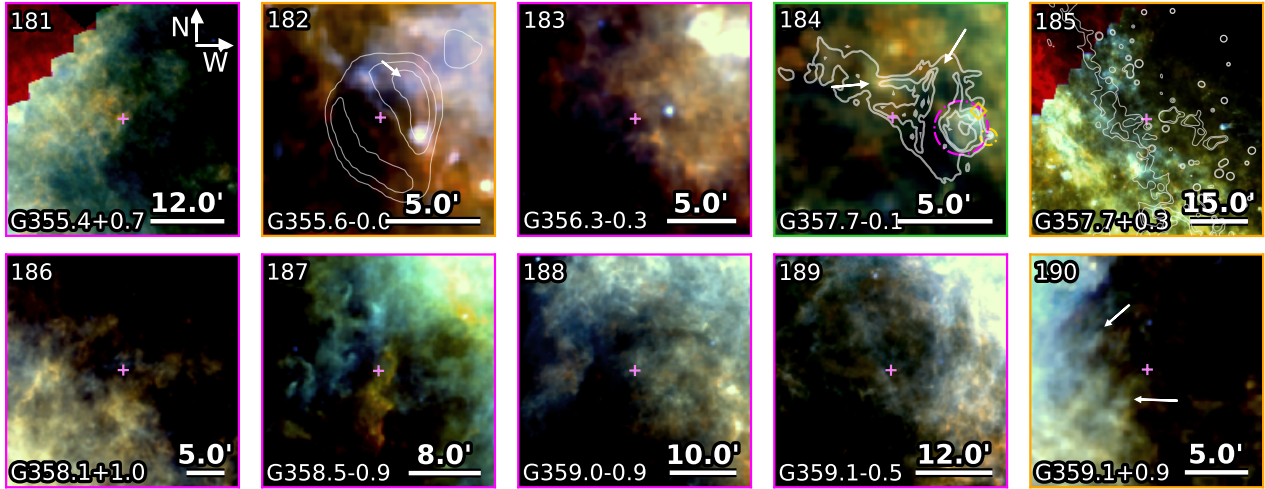


Figure A1 – continued MOST 843 MHz contours are overlaid onto G355.6–0.0; NVSS 1.4 GHz (white) and *Chandra* X-ray (cyan) contours are overlaid onto G357.7–0.1; MIPS 24 μ m contours are overlaid onto G357.7+0.3. The gold diamond overlaid onto the images of G357.7–0.1 and G357.7+0.3 indicate the locations of an OH (1720 MHz) maser and a Mira star respectively.

Table A1. Supernova remnants in the Hi-GAL Survey

SNR	Name	Size ^a (arcmin)	PWN ^b (FIR)	Age (kyr)	SN Type	Hi-GAL ^d	C19 ^e	Dust features ^f	Comparison ^h	References
G0.0+0.0	Sgr A East	3.5x.25	Y (N)	9	Core collapse	2			R	1; 2; 3
G0.3+0.0		15x8				3			R	
G0.9+0.1		8	Y (N)	2 – 3	Core collapse	3			R	4
G1.0–0.1		8				3			R	1
G1.4–0.1		10				3			R	1
G1.9+0.3		1.5		~ 0.1		3			R	5; 6; 7; 8
G3.7–0.2		14x11				4			R	9
G3.8+0.3		18				4			R	9
G5.5+0.3		15x12				3			R	
G6.1+0.5		18x12				4			R	
G6.4–0.1	W28	48		10		1		Filaments	R	10; 1
G6.5–0.4		18				2			R	
G7.0–0.1		15				3			R	
G7.2+0.2		12				3			R	
G8.3–0.0		5x4				1		Shell	R	
G8.7–0.1	W30	45				3			R	1
G8.9+0.4		24				3			R	
G9.7–0.0		15x11				3			R	11; 1
G9.8–0.6		12				3			R	9
G9.9–0.8		12				2			R	
G10.5–0.0		6				2	Y		R	
G11.0–0.0		11x9				3			R	
G11.1–1.0		18x12				1	Y	Shell	OR	
G11.1–0.7		11x7				3	Y		R	
G11.1+0.1		12x10				1	Y	Western shell	R	
G11.2–0.3		4	Y (Y)	1.4 – 2.4	Type cIIb or Ibc	1	Y	Shell	RX	12
								Central region (PWN)		
G11.4–0.1		8				3	Y		R	9
G11.8–0.2		4				3	Y			
G12.0–0.1		7	Y (N)	0.3 – 3.0	Core collapse	3	Y			13
G12.2+0.3		6x5				4			R	
G12.5+0.2		6x5				3	Y		R	
G12.7–0.0		6				2			R	
G12.8–0.0		3		~ 0.34	Core collapse	3			R	14; 15
G13.5+0.2		5x4				1i		Filaments	R	9
G14.1–0.1		6x5				1	Y			
G14.3+0.1		5x4				1	Y	Partial shell	R	
G15.4+0.1		15x14	Y (N)	~ 2.5	Core collapse	3			R	16; 17
G15.9+0.2		7x5		≤ 2.4	Core collapse	1	Y	Partial shell	RX	18; 19
G16.0–0.5		15x10				3			R	20
G16.4–0.5		13				1	Y	Central region	R	
G16.7+0.1		4	Y (N)	2.1	Core collapse	3	Y		R	21; 1
G17.0–0.0		5				3	Y			
G17.4–0.1		6				2	Y		R	9
G18.1–0.1		8		5		3	Y		R	22
G18.6–0.2		6	? (N)	13	Core collapse	1	Y	Outer filaments	R	23

Table A1 – continued Supernova remnants in the Hi-GAL Survey

SNR	Name	Size ^a (arcmin)	PWN ^b (FIR)	Age (kyr)	SN Type	Hi-GAL ^d	C19 ^e	Dust features ^f	Comparison ^g	References
G18.8+0.3	Kes 67	17x11		16		3	Y		R	24
G19.1+0.2		27				3	Y			
G20.0–0.2		10	Y (N)		Core collapse	3	Y		R	25; 26
G20.4+0.1		8		3.6		1	Y	Shell	R	
G21.0–0.4		9x7				3	Y		R	
G21.5–0.9		5	Y (Y)	0.87	Type IIP or Ib/Ic	1	Y	Central region (PWN)	X	26; 27
G21.5–0.1		5				1	Y	Central region	R	
G21.6–0.8		13				3	Y			28
G21.8–0.6	Kes 69	20		5		3	Y		R	29
G22.7–0.2		26	? (N)			3	Y		R	9
G23.3–0.3	W41	27		200		2			R	30; 31; 32
G23.6+0.3		10?				2	Y		R	
G24.7–0.6		15?		6.4		4			R	9
G24.7+0.6		30x15		12		3			R	33
G27.4+0.0	4C-04.7	4		0.75 – 2.1	SN IIL/b	2	Y		R	34; 35
	Kes 73									
G27.8+0.6		50x30	? (N)	35 – 55	Core collapse	4	Y			33; 36
G28.6–0.1		13x9		19		3	Y		R	37
G29.6+0.1		5		< 8		2	Y		R	38; 39
G29.7–0.3	Kes 75	3	Y (Y)	< 0.84	Type Ib/c	1	Y	Central region (PWN) Partial shell	RX	39; 40
G30.7+1.0		24x18				4				9
G31.5–0.6		18?				3				9
G31.9+0.0	3C391	7x5		4		1	Y	Partial shell		41
								Northwestern radio bar		
G32.1–0.9		40?		12		3			R	42
G32.4+0.1		6				3	Y			43
G32.8–0.1	Kes 78	17		6		3	Y			44; 45
G33.2–0.6		18				1	Y	Western shell	R	9
G33.6+0.1	Kes 79	10		4.4 – 6.7	Type II	2	Y		R	45; 46
G34.7–0.4	W44	35x27	Y (N)	2	Core collapse	1	Y	North and western shell Central filaments	R	47; 48
G35.6–0.4		15x11		2.3		2	Y		R	48; 49
G36.6–0.7		25?				3			R	
G39.2–0.3	3C396	8x6	Y (N)	7		1	Y	Western shell	R	49; 50
G40.5–0.5		22				3			R	51
G41.1–0.3	3C397	4.5x2.5		1.35 – 1.75	Type Ia	3	Y		R	50; 52
G41.5+0.4		10	? (N)			3			R	53
G42.0–0.1		8				3			R	
G42.8+0.6		24				4				9
G43.3–0.2	W49B	4x3		1 – 4	Bipolar Ib/Ic	1	Y	Fe/radio loop H_2 filament	R	54; 55; 56; 57
G45.7–0.4		22				3			R	9
G46.8–0.3	(HC30)	30				3			R	58
G49.2–0.7	(W51)	30	Y (?)	30	Core collapse	4				59; 60; 61; 1
G54.1+0.3		12?	Y (Y)	2	Core collapse	1	Y	PWN southern rim		62

Table A1 – continued Supernova remnants in the Hi-GAL Survey

SNR	Name	Size ^a (arcmin)	PWN ^b (FIR)	Age (kyr)	SN Type	Hi-GAL ^d	C19 ^e	Dust features ^f	Comparison ^g	References
G54.4–0.3	(HC40)	40		95		1	Y	Outer filaments		63
G55.0+0.3		20x15?		≤ 1900		2	Y			64
G57.2+0.8		12?	? (N)			3			R	65
G59.5+0.1		15		86		3				66; 67
G64.5+0.9		8				3				68
G65.1+0.6		90x50	? (?)	40 – 140	Core collapse	3				68
G65.8–0.5		10x6?				1		Eastern structure	OR	69
G66.0–0.0		31x25?				4				
G67.6+0.9		50x45?				3		Partial shell	OR	
G67.8+0.5		7x5				1			R	9
G69.7+0.9		16x14				3			R	
G73.9+0.9		27				3			R	
G76.9+1.0		9	? (N)	< 40	Core collapse	3			R	70
G83.0–0.3		9x7				-				
G84.2–0.8		20x16		9		-				71
G85.4+0.7		24?			Core collapse	3			R	72
G85.9–0.6		24			Type Ia	-				72
G93.7–0.2		80				-				73
G94.0+1.0	3C434.1	30x25		7.9	Core collapse	3			R	74
G108.2–0.6		70x54				-				31
G109.1–1.0		28		14		-				75; 76
G113.0+0.2		40x17				-				77
G114.3+0.3		90x55		7.7	Core collapse	3			R	78
G116.9+0.2	CTB 1	34		13.1	Core collapse	4			R	78; 79; 80
G127.1+0.5	R5	45		20 – 30		3			R	81
G205.5+0.5	Monoceros Nebula	220		30		-				82; 83
G213.0–0.6		160x140				-				84
G289.7–0.3		18x14				3			R	9
G290.1–0.8	MSH 11-61A	19x14	Y (N)	50	Core collapse	3			R	85; 86
G291.0–0.1	(MSH 11-62)	15x13		~ 1.3	Core collapse	3			R	87; 88
G292.2–0.5		20x15	Y (N)	1.7	Core collapse	3			X	
G293.8+0.6		20				-				
G294.1–0.0		40				3			R	
G296.1–0.5		37x25		28	Core collapse	3			R	89; 90
G296.7–0.9		15x8				3			R	
G296.8–0.3	1156-62	20x14		2 – 10		3	Y		R	91
G298.5–0.3		5?				3			R	92
G298.6–0.0		12x9				1		Outer filaments	XR	93
G299.6–0.5		13				3			R	9
G301.4–1.0		37x23				3			R	9
G302.3+0.7		17				3			R	9
G304.6+0.1	Kes 17	8		28 – 64	Core collapse	1	Y	Western shell	R	94
G306.3–0.9		4		2.3	Type Ia	1		Inner region	XR	95; 96
G308.1–0.7		13				3			R	9
G308.8–0.1		30x20?		≤ 32.5	Core collapse	3			R	97; 98
G309.2–0.6		15x12		0.7 – 4		3			R	99

Table A1 – continued Supernova remnants in the Hi-GAL Survey

SNR	Name	Size ^a (arcmin)	PWN ^b (FIR)	Age (kyr)	SN Type	Hi-GAL ^d	C18 ^e	Dust features ^f	Comparison ^g	References
G309.8+0.0		25x19				2		Shell	R	100
G310.6–0.3	Kes 20B	8				3	Y		R	9
G310.8–0.4	Kes 20A	12				1	Y		R	101
G311.5–0.3		5		25 – 42		1	Y	Shell		102
G312.4–0.4		38		50	Core collapse	3			R	103
G315.4–0.3		24x13				3			O	9
G315.9–0.0	The Frying Pan	245x14	Y (N)	10	Core collapse	3			R	104; 105
G316.3–0.0	(MSH 14-57)	29x14				3			R	106
G317.3–0.2		11				3			R	9
G318.2+0.1		40x35				3			R	
G318.9+0.4		30x14				3			R	
G321.9–0.3		31x23				3			R	9
G322.1+0.0		8x4.5?		4.6		3			RX	107
G322.5–0.1		15				3			R	108
G323.5+0.1		13				3			R	9
G327.2–0.1		5		≤ 1.4		3				108
G327.4+0.4	Kes 27	21		2.4 or 5.3		3			R	109
G327.4+1.0		14				3			R	9
G328.4+0.2	(MSH 15-57)	5	Y (N)	10	Core collapse	3				109
G329.7+0.4		40x33				3			R	
G330.2+1.0		11		3.1	Core collapse	3			R	109; 110
G332.0+0.2		12				3	Y			
G332.4–0.4	RCW 103	10		2	Type IIP	1	Y	Southern arc	X	111; 112
G332.4+0.1	MSH 16-51	15		3		3	Y			113
	Kes 32									
G335.2+0.1		21				3			R	114
G336.7+0.5		14x10				3	Y		R	9
G337.0–0.1		21		70		3			R	115; 116
G337.2–0.7		6		0.75 – 3.5	Type Ia	2	Y		RX	117; 118
G337.2+0.1		3x2	Y (N)	1.5	Core collapse	3			R	119
G337.3+1.0	Kes 40	15x12				3			R	9
G337.8–0.1	Kes 41	9x6		3.3		3			R	120; 121
G338.1+0.4		15?				3			R	9
G338.3–0.0		8	Y (N)	6.8	Core collapse	3			R	122; 123
G338.5+0.1		9		5 – 17		3			R	124; 17
G340.4+0.4		10x7		3.1		3	Y		R	125
G340.6+0.3		6		2.6		1	Y	Shell	R	125
G341.2+0.9		22x16	Y (N)	32.6	Core collapse	3	Y			126
G341.9–0.3		7		5		3	Y			125
G342.0–0.2		12x9		11.7		3	Y		R	125; 9
G342.1+0.9		10x9				3				9
G343.1–0.7		27x21				3			R	9
G344.7–0.1		8		3	Type Ia	1	Y	North-central region	XR	127; 128
G345.7–0.2		6				2	Y		R	9
G346.6–0.2		8		47	Type Ib/Ic/II	2	Y		R	129; 1
G347.3–0.5	RX J1713.7-3946	65x55		1.59 – 2.1	Type Ib/c	3	Y			130

Table A1 – continued Supernova remnants in the Hi-GAL Survey

SNR	Name	Size ^a (arcmin)	PWN ^b (FIR)	Age (kyr)	SN Type	Hi-GAL ^d	C19 ^e	Dust features ^f	Comparison ^g	References
G348.5–0.0		10?				1	Y	Arc	R	129
G348.5+0.1	CTB37A	15?	? (N)	32 – 42		1	Y	Northern arc	R	131; 129; 1
G348.7+0.3	CTB 37B	17?		5	Core collapse	1	Y	Breakout region	R	132
G349.2–0.1		9x6				4	Y	North-eastern shell	R	
G349.7+0.2		2.5x2		1.8	Core collapse	1	Y	Eastern shell	R	133; 134; 1
G350.1–0.3		4?		0.6 – 1.2	Core collapse	1		Ejecta region	R	135; 136; 134
G351.2+0.1		7				1		Northern bar and central region	R	137
G351.7+0.8		18x14		≤ 68		3			R	138
G351.9–0.9		12x9				3			R	
G352.7–0.1		8x6		1.6	Type Ia	3			R	139; 140; 141
G353.6–0.7	HESS J1731-347	30		2 – 6	Core collapse	3			R	75; 142; 143
G354.1+0.1		15x3		26	Core collapse	2			R	126
G354.8–0.8		19				3			R	9
G355.4+0.7		25				3			R	
G355.6–0.0		8x6		20		2			R	9; 144
G356.3–0.3		11x7				3			R	9
G357.7–0.1	MSH 17-39 The Tornado	8x3?				1		Head and tail regions	R	1
G357.7+0.3	The Square Nebula	24		≤ 6.4		2			R	145; 1
G358.1+1.0		20				3			R	
G358.5–0.9		17				3			R	
G359.0–0.9		23				3			R	9
G359.1–0.5		24		≥ 100		3			R	1; 146
G359.1+0.9		12x11				2			R	9

^a Radio size from Green's catalogue. ^b ‘Y’ indicates that a source contains an associated PWN, ‘?’ indicates an unconfirmed PWN candidate. FIR detection of the PWN is indicated in brackets. Level of detection for each SNR is listed for the following surveys: ^d *Herschel* Hi-GAL (PACS & SPIRE, C19 and this work); ‘-’ indicates that the source is not covered by the HiGAL survey. ^e Sources marked with ‘Y’ were studied by C19. ^f Location of FIR detected dust features. ^g Waveband of previous detection to which FIR structure is compared: O = optical, R = radio, X = X-ray.

References for age and SN type: ¹Pihlström et al. 2014, ²Zhao et al. 2013, ³Nynka et al. 2013, ⁴Camilo et al. 2009a, ⁵Carlton et al. 2011, ⁶Roy & Pal 2013, ⁷Borkowski et al. 2014, ⁸Zoglauer et al. 2015, ⁹Case & Bhattacharya 1998, ¹⁰Rho & Borkowski 2002, ¹¹Hewitt & Yusef-Zadeh 2009, ¹²Borkowski et al. 2016, ¹³Yamauchi et al. 2014, ¹⁴Halpern et al. 2012, ¹⁵Brogan et al. 2005, ¹⁶Castelletti et al. 2013, ¹⁷HESS Collaboration 2014, ¹⁸Reynolds 2006, ¹⁹Klochkov et al. 2016, ²⁰Beaumont et al. 2011, ²¹Helfand et al. 2003, ²²Leahy et al. 2014, ²³Voisin et al. 2016, ²⁴Dubner et al. 1999, ²⁵Petriella et al. 2013, ²⁶Bietenholz & Bartel 2008, ²⁷Bocchino et al. 2005, ²⁸Bietenholz et al. 2011, ²⁹Tian & Leahy 2008, ³⁰Leahy & Tian 2008, ³¹Tian et al. 2007b, ³²HESS Collaboration 2015, ³³Reich et al. 1984, ³⁴Kumar et al. 2014, ³⁵Chevalier 2005, ³⁶Misanovic et al. 2010, ³⁷Bamba et al. 2001, ³⁸Gaensler et al. 1999, ³⁹Leahy et al. 2008, ⁴⁰Morton et al. 2007, ⁴¹Chen et al. 2004, ⁴²Folgeraiter et al. 1997, ⁴³Yamaguchi et al. 2004, ⁴⁴Zhou & Chen 2011, ⁴⁵Zhou et al. 2016, ⁴⁶Sato et al. 2016, ⁴⁷Wolszczan et al. 1991, ⁴⁸Zhu et al. 2013, ⁴⁹Harris & Slane 1999, ⁵⁰Leahy & Ranasinghe 2016, ⁵¹Downes et al. 1980, ⁵²Yamaguchi et al. 2015, ⁵³Hurley et al. 1999, ⁵⁴Pye et al. 1984, ⁵⁵Smith et al. 1985, ⁵⁶Hwang et al. 2000, ⁵⁷Lopez et al. 2013, ⁵⁸Sato 1979, ⁵⁹Koo et al. 1995, ⁶⁰Koo & Moon 1997, ⁶¹Green et al. 1997, ⁶²Bocchino et al. 2010, ⁶³Park et al. 2013, ⁶⁴Matthews et al. 1998, ⁶⁵Surnis et al. 2016, ⁶⁶Billot et al. 2010, ⁶⁷Xu & Wang 2012, ⁶⁸Tian & Leahy 2006, ⁶⁹Shan et al. 2018, ⁷⁰Arzoumanian et al. 2011, ⁷¹Leahy & Green 2012, ⁷²Jackson et al. 2008, ⁷³Uyaniker et al. 2002, ⁷⁴Jeong et al. 2013, ⁷⁵Tian et al. 2010, ⁷⁶Sasaki et al. 2013, ⁷⁷Kothes et al. 2005, ⁷⁸Yar-Uyaniker et al. 2004, ⁷⁹Lazendic & Slane 2006, ⁸⁰Pannuti et al. 2010, ⁸¹Leahy & Tian 2006, ⁸²Odegard 1986, ⁸³Leahy et al. 1986, ⁸⁴Reich et al. 2003, ⁸⁵Reynoso et al. 2006, ⁸⁶Kamitsukasa et al. 2015, ⁸⁷Moffett et al. 2002, ⁸⁸Slane et al. 2012, ⁸⁹Castro et al. 2011, ⁹⁰Gök & Sezer 2012, ⁹¹Gaensler et al. 1998, ⁹²Hwang & Markert 1994, ⁹³Bamba et al. 2016, ⁹⁴Combi et al. 2010, ⁹⁵Reynolds et al. 2013, ⁹⁶Combi et al. 2016, ⁹⁷Caswell et al. 1992, ⁹⁸Kaspi et al. 1992, ⁹⁹Rakowski et al. 2001, ¹⁰⁰Caswell et al. 1980, ¹⁰¹Andersen et al. 2011, ¹⁰²Pannuti et al. 2014a, ¹⁰³Doherty et al. 2003, ¹⁰⁴Camilo et al. 2009b, ¹⁰⁵Ng et al. 2012, ¹⁰⁶Caswell et al. 1975, ¹⁰⁷Heinz et al. 2013, ¹⁰⁸Whiteoak 1992, ¹⁰⁹McClure-Griffiths et al. 2001, ¹¹⁰Torii et al. 2006, ¹¹¹Nugent et al. 1984, ¹¹²Frank et al. 2015, ¹¹³Vink 2004, ¹¹⁴Kaspi et al. 1996, ¹¹⁵Sarma et al. 1997, ¹¹⁶Castro et al. 2013, ¹¹⁷Rakowski et al. 2006, ¹¹⁸Takata et al. 2016, ¹¹⁹Combi et al. 2005, ¹²⁰Combi et al. 2008, ¹²¹Zhang et al. 2015, ¹²²Lemiere et al. 2009, ¹²³Gotthelf et al. 2014, ¹²⁴Kothes & Dougherty 2007, ¹²⁵Caswell et al. 1983, ¹²⁶Frail et al. 1994, ¹²⁷Giacani et al. 2011, ¹²⁸Yamaguchi et al. 2012, ¹²⁹Pannuti et al. 2014a, ¹³⁰Tsuji & Uchiyama 2014, ¹³¹Tian & Leahy 2012, ¹³²HESS Collaboration 2008b, ¹³³Tian & Leahy 2014, ¹³⁴Yasumi et al. 2014, ¹³⁵Gaensler et al. 2008, ¹³⁶Lovichinsky et al. 2011, ¹³⁷Dubner et al. 1993, ¹³⁸Tian et al. 2007a, ¹³⁹Giacani et al. 2009, ¹⁴⁰Pannuti et al. 2014b, ¹⁴¹Sezer & Gök 2014, ¹⁴²HESS Collaboration 2011, ¹⁴³Acero et al. 2015, ¹⁴⁴Minami et al. 2013, ¹⁴⁵Phillips & Marquez-Lugo 2010, ¹⁴⁶HESS Collaboration 2008a.

APPENDIX B: DUST TEMPERATURES IN THE LEVEL 1 DETECTED SUPERNOVA REMNANTS

B1 SNR Temperature Map Simulations

Due to the location of the Galactic Plane SNRs, there is significant contamination from foreground/background interstellar emission for most of our sample and many of the sources (even the level 1 detections) are faint in comparison to the surrounding or foreground/background ISM. As such, any dust temperatures and dust masses derived could be significantly affected by this issue, more so than in studies of SNRs in the Large Magellanic Cloud which is a face-on galaxy. This is the biggest limitation when attempting to measure dust masses and temperatures in a statistical sample of Galactic SNe.

We test the effect of this by simulating a dusty SNR for a bright and faint case. Both simulated SNRs with varying temperatures have the same 70/160 colours, but the former is chosen to be high signal-to-noise, well above the brightness of the ISM (the simulated SNR has pixel fluxes up to $\sim 9,000$ MJy/sr and ~ 3200 MJy/sr at 70 and 160 μm respectively compared with an average ISM value of ~ 390 and ~ 1370 MJy/sr), and the latter is at a similar level to the brightness of IS clouds seen at off-SNR points in our HiGAL maps (with 70 μm fluxes in the SNR ~ 10 times fainter than the bright case). Our simulation consists of a SNR with an outer shell of dust with temperature 65 K (to simulate dust heated in forward shock regions) and two cooler components of ejecta dust (at 25 K and 37 K) to simulate cooler ejecta dust similar to the observed PWNe remnants (Chawner et al. 2019) and a Cassiopeia A-like SNR (Barlow et al. 2010; De Looze et al. 2017).

Using Equation 1 on the simulated SNR recovers the input temperatures perfectly. The simulated source is then placed onto a region of the HiGAL survey at $\alpha = 18^{\text{h}}07^{\text{m}}58^{\text{s}}$, $\delta = -19^{\circ}27'16''$ ($l = 10.7537$, $b = 0.364$) as shown in the top panels of Figure B1, this region is chosen as there is a large variation in the background level, as is the case for several of our level 1 detected SNRs. Equation 1 is then used to create the dust temperature map. The output dust temperatures are significantly biased towards lower temperatures than the input simulation. Across the map, the dust temperatures are lower by 5–15 K compared to the simulated source, simply as a result of placing the simulated SNR onto a region with background interstellar emission. This situation is further compounded if we take the fainter simulated SNR (which is much more comparable to our real detection level 1 sources). Here the output temperatures range from 20–30 K compared to the input 20–65 K, with an offset of 30 K in the shell. For the faint source simulation, we also see more variation in the output shell temperatures compared to the bright source. It is clear that for fainter dusty SNRs, the ISM contamination affects the output dust temperatures by significant amounts (and ultimately could lead to orders of magnitude errors in any estimate of the dust mass, depending on the dust size and composition).

To address this we test the affects of attempting to remove the background level and re-derive the temperatures using Equation 1 on the background subtracted 70–160 μm simulated images. The background level for the simulated SNR is estimated, and then subtracted, using the Nebuliser

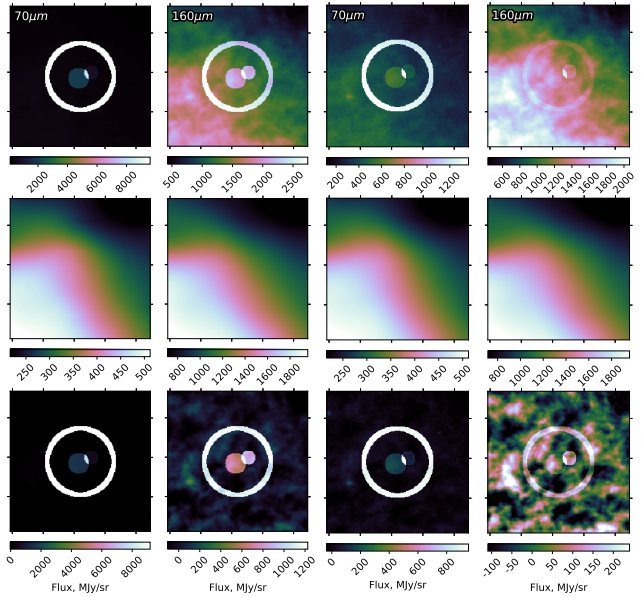


Figure B1. Background subtraction using the Nebuliser routine applied to the bright simulated source (left) and the less bright case (right). *Top:* images prior to background subtraction, *middle:* background estimated by Nebuliser, and *bottom:* background subtracted image.

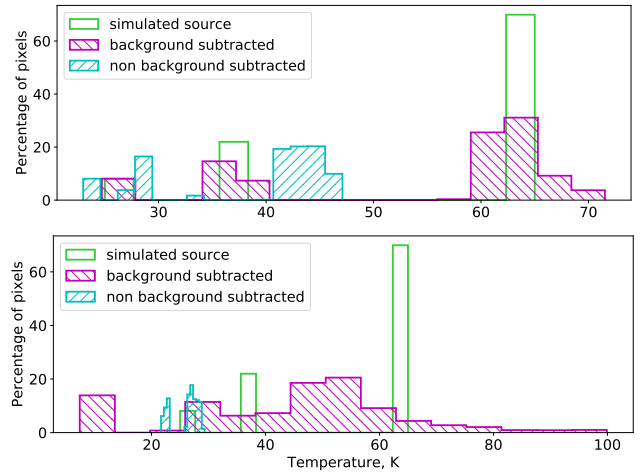


Figure B2. Temperatures within the simulated source in the case of a bright simulated source (*top*) and a less bright source (*bottom*). In both cases we find a distribution which is much more similar to the input when we apply a background subtraction.

routine¹ from the CASUTools suite. Nebuliser takes a region around the SNR to model large scale variations in the ISM level and then subtract this to return a map with a zero average. We use Nebuliser as it allows us to model variations in the ISM level, rather than assuming a constant level which does not accurately represent the entire region. Nebuliser is applied to the 70 and 160 μm images for our simulated SNR,

¹ <http://casu.ast.cam.ac.uk/surveys-projects/software-release/background-filtering>

producing the image shown in [Figure B1](#), and Equation 1 is then used on the Nebuliser subtracted 70 and 160 μm maps.

For our bright SNR we find that the output temperature map after background subtraction accurately recovers the majority of the input temperatures across the full range of the simulated data (see [Figure B2](#)). An improvement is also seen for the fainter simulated SNR as we are able to identify both warm and cool dust where before we were limited to a very narrow range of cool temperatures. The resulting temperature distribution after background subtraction is wider compared with the input temperatures, as the contamination of the ISM dust in the pixels at a similar brightness level to the simulated SNR has led to a smearing out of the dust temperatures. We also see that for the faint case, the output temperature map is more sensitive to Nebuliser's modeling of large scale variations in the ISM, there are more small scale features in the output map than in the original simulation.

B2 Notes on the Temperature Maps for Individual Remnants

In this section we study the SNR temperature maps in [Figure 21](#) which are produced using the 70–160 μm flux ratio after background subtraction, as discussed above. We compare with multi-waveband images to identify the source of elevated dust temperatures, which can be an indicator of heating sources such as ISM–SNR interactions. Because of arbitrary colour scaling in Section 2, some warm dust features may not be evident in the *Herschel* false colour images, but may be revealed here.

G8.3–0.0: Broad molecular emission (^{12}CO), flattened radio contours, a possible OH maser, and a gamma-ray source all suggest interaction with molecular cloud to the north-west ([Higashi et al. 2008; Kilpatrick et al. 2016](#)). We detect warm dust between ~ 27 and 33 K at the same location of the broad molecular lines observed by [Kilpatrick et al. \(2016\)](#) (their Figure 5) where it is expected that there is a SNR-MC interaction, suggesting that this is heating the dust in this region.

G11.1+0.1: We find evidence of warm dust (~ 24 – 30 K) in the region of this SNR and dust within the magenta circle in [Figure 21](#) to the north is found within the radio contours. The warmest material, towards the south, does not correlate with the radio structure.

G16.4–0.5: There is warm dust (~ 23 – 28 K), the warmest of which is offset to the north-east of the 70 μm bright region, indicated by the magenta circle in [Figure 21](#). The warm dust is in a similar location to radio structure although its morphology differs making it difficult to determine if the origin of the two is the same.

We do not see evidence that the *Herschel* shell around the south and western extent of the SNR has any variation in temperature compared with unrelated dust in the region.

G20.4+0.1: We find some warm dust (~ 25 – 27 K) that correlates with the radio structure, although the majority of the warm material has a different structure or is found outside of the radio contours. [Anderson et al. \(2011\)](#) suggested

that this source may be a HII region (G20.479+0.165, [Lockman 1989](#)).

G21.5–0.1: There is evidence of warm dust (~ 23 – 30 K) in this SNR although it does not seem to correlate with the radio structure, as shown in [Figure 21](#). The warmest region within the radio contours is found in the central region, in a gap in the 160 μm structure. There is also warm dust at the edge of the south-eastern radio contours which may be swept up or shock-heated material if it is associated with the SNR.

W49B, G43.3–0.2: Numerous studies of CO, HI, shocked H₂, and MIR emission indicate that this SNR is interacting with molecular clouds ([Reach et al. 2006; Zhu et al. 2014; Kilpatrick et al. 2016](#)), although this is not completely clear as opposing studies find a lack of evidence for molecular material around the SNR ([Lacey et al. 2001; Ranasinghe & Leahy 2018](#)).

Our analysis supports the argument that there is some interaction as we detect warm dust (up to $\sim 36\text{ K}$) which coincides with the expected location of interactions to the east and south-west.

We also detect warm (~ 29 – 32 K) dust from a filament at $\alpha = 19^{\text{h}}11^{\text{m}}07^{\text{s}}$, $\delta = +09^{\circ}07'01''$ from which MIR colours suggest line emission from ionic shocks ([Reach et al. 2006](#)).

G65.8–0.5: We find evidence of warm dust (~ 24 – 32 K) towards the east of the remnant, at the location of the H α structure discussed in Section 2.1. *Herschel* 160–500 μm emission was detected from a structure towards the radio centre of the SNR in Section 2.1 this region has temperatures between ~ 20 and 22 K .

G67.8+0.5: There is some evidence of anti-correlation between the radio contours and the dust temperatures. A warm ($\sim 38\text{ K}$) region of dust lies in the region between two radio peaks towards the west of the remnant, as shown by the contours in [Figure 21](#). There is also a peak of warm dust near the centre of the SNR which is located in a gap in the brightest radio structure. The origin of the warm dust is unclear as there is limited observations of this source. If the material is associated with the SNR it could be warm ejecta material, reverse-shocked material, or evidence of dust destruction.

We do not see evidence of warm dust at the location of optical emission to the west, where there is a potential bow shock ([Sabin et al. 2013](#)).

Kes 20A, G310.8–0.4: *Spitzer* Infrared Spectrograph (IRS) observations to the south-east suggest that this SNR has a relatively low velocity shock (~ 35 – 70 km s^{-1}) into a low-density medium ($\sim 10^3 \text{ cm}^{-3}$) and has a distribution of dust grains that indicates shattering of grains in the shock ([Andersen et al. 2011](#)). We do not see evidence for dust in the south-east region that is significantly warmer than the surrounding ISM. The warmest dust identified in this source is towards the north, at the location of FIR and radio structure. If this warm dust is associated with the SNR the correlation with radio could indicate shock-heated dust in this region.

G340.6+0.3: Elemental abundances indicate that ejecta dominates the X-ray bright northern shell, whereas the emission in the south is from shocked ISM (Mangano et al. 2014). We find evidence of warm dust (~ 25 – 30 K) in the northern arc with a peak in the north-east, slightly offset from the X-ray contours, which may be warm ejecta dust. There is also warm dust in the south in a region of bright X-ray emission, although the warmest dust in this area is offset from the brightest X-ray structures. Because of the coincidence we expect that the warm dust is also shocked ISM.

G349.7+0.2: There is evidence from OH (1720 MHz) masers (Frail et al. 1996) (see the yellow diamonds in ??) and line emission (Reynoso & Mangum 2000; Lazendic et al. 2010) that this SNR is interacting with a coincident molecular cloud (Dubner et al. 2004). Although there is bright *Herschel* emission towards the central interacting region, our analysis suggests that the warmest dust is offset to the east.

The SNR is expanding at $\sim 710 \text{ km s}^{-1}$ (Lazendic et al. 2005) into a medium with a density gradient, where the density is relatively low towards the west and higher towards the east. Corresponding to this gradient, we find warmer material in the eastern region where the SNR is dominated by swept-up medium (Lazendic et al. 2005), whereas towards the west we do not see evidence for SNR material that is noticeably warmer than the surrounding ISM. It is likely that the warm dust in the east of the remnant is swept-up material.

REFERENCES

- Acero F., Renaud M., Ballet J., Hewitt J. W., Rousseau R., Tanaka T., 2015, A&A, 580, A74
- Andersen M., Rho J., Reach W. T., Hewitt J. W., Bernard J. P., 2011, ApJ, 742, 7
- Anderson L. D., Bania T. M., Balser D. S., Rood R. T., 2011, ApJ SS, 194
- Arzoumanian Z., Gotthelf E. V., Ransom S. M., Kothes R., Landecker T. L., 2011, ApJ, 739
- Bamba A., Ueno M., Koyama K., Yamauchi S., 2001, PASJ, 53, 21
- Bamba A., Sawada M., Nakano Y., Terada Y., Hewitt J., Petre R., Angelini L., 2016, PASJ, 68, S51
- Barlow M. J., et al., 2010, A&A, 518, L138
- Beaumont C. N., Williams J. P., Goodman A. A., 2011, AJ, 741
- Bietenholz M. F., Bartel N., 2008, MNRAS, 386, 1411
- Bietenholz M. F., Matheson H., Safi-Harb S., Brogan C., Bartel N., 2011, MNRAS, 412, 1221
- Billot N., Noriega-Crespo A., Carey S., Guieu S., Shenoy S., Paladini R., Latter W., 2010, ApJ, 712, 797
- Bocchino F., van der Swaluw E., Chevalier R., Bandiera R., 2005, A&A, 442, 539
- Bocchino F., Bandiera R., Gelfand J., 2010, A&A, 71, 1
- Borkowski K. J., Reynolds S. P., Green D. A., Hwang U., Petre R., Krishnamurthy K., Willett R., 2014, ApJ Letters, 790, 18
- Borkowski K. J., Reynolds S. P., Roberts M. S. E., 2016, ApJ, 819, 160
- Brogan C. L., Gaensler B. M., Gelfand J. D., Lazendic J. S., Lazio T. J. W., Kassim N. E., McClure-Griffiths N. M., 2005, ApJ, 629, L105
- Camilo F., Ransom S. M., Gaensler B. M., Lorimer D. R., 2009a, ApJ, 700, 34
- Camilo F., Ng C. Y., Gaensler B. M., Ransom S. M., Chatterjee S., Reynolds J., Sarkissian J., 2009b, ApJ, 703, 55
- Carlton A. K., Borkowski K. J., Reynolds S. P., Hwang U., Petre R., Green D. A., Krishnamurthy K., Willett R., 2011, ApJ Letters, 737, L22
- Case G. L., Bhattacharya D., 1998, ApJ, 504, 761
- Castelletti G., Supan L., Dubner G., Joshi B., Surnis M., 2013, A&A, 557, L15
- Castro D., Slane P. O., Gaensler B. M., Hughes J. P., Patnaude D. J., 2011, ApJ, 734, 86
- Castro D., Slane P., Carlton A., Figueroa-Feliciano E., 2013, ApJ, 774
- Caswell J. L., Murray J. D., Roger R. S., Cole D. J., Cooke D. J., 1975, A&A, 45, 239
- Caswell J. L., Haynes R. F., Milne D. K., Wellington K. J., 1980, MNRAS, 190, 881
- Caswell J. L., Haynes R. F., Milne D. K., Wellington K. J., 1983, MNRAS, 203, 595
- Caswell J. L., Kesteven M. J., Stewart R. T., Milne D. K., Haynes R. F., 1992, ApJ, 399, L151
- Chawner H., et al., 2019, MNRAS, 483, 70
- Chen Y., Su Y., Slane P. O., Wang Q. D., 2004, ApJ, 616, 27
- Chevalier R. a., 2005, ApJ, 619, 839
- Combi J. A., Benaglia P., Romero G. E., Sugizaki M., 2005, A&A, 431, L9
- Combi J. A., Albacete Colombo J. F., Martí J., 2008, A&A, 28, L25
- Combi J. A., et al., 2010, A&A, 523, A76
- Combi J. A., García F., Suárez A. E., Luque-Escamilla P. L., Paron S., Miceli M., 2016, A&A, 592, 8
- De Looze I., et al., 2017, MNRAS, 465, 3309
- Doherty M., Johnston S., Greeb A. J., Roberts M. S., Romani R. W., Gaensler B. M., Crawford F., 2003, MNRAS, 339, 1048
- Downes A. J. B., Pauls T., Salter C. J., 1980, A&A, 92, 46
- Dubner G. M., Moffett D. A., Goss W. M., Winkler P. F., 1993, AJ, 105, 2251
- Dubner G., Giacani E., Reynoso E., 1999, AJ, 118, 930
- Dubner G., Giacani E., Reynoso E., Parón S., 2004, A&A, 426, 201
- Folgheraiter E. L., Warwick R. S., Watson M. G., Koyama K., 1997, MNRAS, 292, 365
- Frail D. A., Goss W. M., Whiteoak J. B. Z., 1994, AJ, 437, 23
- Frail D. A., Reynoso E., Giacani E., Green A., Otrupcek R., 1996, AJ, 111, 1651
- Frank K. A., Burrows D. N., Park S., 2015, AJ, 810, 113
- Gaensler B. M., Manchester R. N., Green A. J., 1998, MNRAS, 296, 813
- Gaensler B. M., Gotthelf E. V., Vasisht G., 1999, ApJ, 526, L37
- Gaensler B. M., et al., 2008, ApJ, 680, L37
- Giacani E., Smith M. J. S., Dubner G., Loiseau N., Castelletti G., Paron S., 2009, A&A, 507, 841
- Giacani E., Smith M. J. S., Dubner G., Loiseau N., 2011, A&A, 531, A138
- Gök F., Sezer A., 2012, MNRAS, 419, 1603
- Gotthelf E. V., et al., 2014, ApJ, 788, 1
- Green D. A., 2014, BASI, 42, 47
- Green A. J., Frail D. A., Goss W. M., Otrupcek R., 1997, ApJ, 114, 2058
- HESS Collaboration 2008a, A&A, 517, 509
- HESS Collaboration 2008b, A&A, 836, 829
- HESS Collaboration 2011, A&A, 531, A81
- HESS Collaboration 2014, ApJ Letters, 794, 2
- HESS Collaboration 2015, A&A, 574, A27
- Halpern J. P., Gotthelf E. V., Camilo F., 2012, ApJ Letters, 753, 10
- Harris I. M., Slane P. O., 1999, ApJ, 516, 811
- Heinz S., et al., 2013, ApJ, 779

- Helfand D. J., Agueros M. A., Gotthelf E. V., 2003, *ApJ*, 592, 941
- Hewitt J. W., Yusef-Zadeh F., 2009, *ApJ*, 694, 16
- Higashi Y., et al., 2008, *ApJ*, 683, 957
- Hurley K., et al., 1999, *ApJ*, 510, L111
- Hwang U., Markert T. H., 1994, *ApJ*, 431, 819
- Hwang U., Petre R., Hughes J. P., 2000, *ApJ*, 532, 970
- Jackson M. S., Safi-Harb S., Kothes R., Foster T., 2008, *ApJ*, 674, 936
- Jeong I. G., Koo B. C., Cho W. K., Kramer C., Stutzki J., Byun D. Y., 2013, *ApJ*, 770
- Kamitsukasa F., Koyama K., Uchida H., Nakajima H., Hayashida K., Mori K., Katsuda S., Tsunemi H., 2015, *PASJ*, 67, 161
- Kaspi V. M., Manchester R. N., Johnston S., Lyne A. G., D'Amico N., 1992, *ApJ*, 399, L155
- Kaspi V. M., Manchester R. N., Johnston S., Lyne A. G., D'Amico N., 1996, *AJ*, 111, 2028
- Kilpatrick C. D., Bieging J. H., Rieke G. H., 2016, *ApJ*, 816, 1
- Klochkov D., Suleimanov V., Sasaki M., Santangelo A., 2016, *A&A*, 12, 8
- Koo B.-C., Moon D.-S., 1997, *ApJ*, 485, 263
- Koo B.-C., Kim K.-T., Seward F. D., 1995, *ApJ*, 447, 211
- Kothes R., Dougherty S. M., 2007, *A&A*, 460, 993
- Kothes R., UyanÄsker B., Reid R. I., 2005, *A&A*, 444, 871
- Kumar H. S., Safi-Harb S., Slane P. O., Gotthelf E. V., 2014, *ApJ*, 781, 41
- Lacey C. K., Lazio T. J. W., Kassim N. E., Duric N., Briggs D., Dyer K. K., 2001, *ApJ*, 559, 954
- Lazendic J. S., Slane P. O., 2006, *ApJ*, 647, 350
- Lazendic J. S., Slane P. O., Hughes J. P., Chen Y., Dame T. M., 2005, *ApJ*, 618, 733
- Lazendic J. S., Wardle M., Whiteoak J. B., Burton M. G., Green A. J., 2010, *MNRAS*, 409, 371
- Leahy D. A., Green K. S., 2012, *ApJ*, 760, 4
- Leahy D. A., Ranasinghe S., 2016, *ApJ*, 817, 74
- Leahy D., Tian W., 2006, *A&A*, 257, 251
- Leahy D. A., Tian W. W., 2008, *AJ*, 135, 167
- Leahy D., Naranan S., Singh K., 1986, *MNRAS*, 220, 501
- Leahy D. A., Tian W., Wang Q. D., 2008, *ApJ*, 136, 1477
- Leahy D., Green K., Tian W., 2014, *MNRAS*, 438, 1813
- Lemiere A., Slane P., Gaensler B. M., Murray S., 2009, *ApJ*, 706, 1269
- Lockman F. J., 1989, *ApJSS*, 71, 469
- Lopez L. A., Ramirez-Ruiz E., Castro D., Pearson S., 2013, *ApJ*
- Lovchinsky I., Slane P., Gaensler B. M., Hughes J. P., Ng C. Y., Lazendic J. S., Gelfand J. D., Brogan C. L., 2011, *ApJ*, 731
- Mangano V., Burrows D. N., Park S., Shea T. K., 2014, in AAS/High Energy Astrophysics Division #14. AAS/High Energy Astrophysics Division. p. 120.05
- Matthews B., Wallace B., Taylor A., 1998, *ApJ*, 20, 312
- McClure-Griffiths N. M., Green a. J., Dickey J. M., Gaensler B. M., Haynes R. F., Wieringa M. H., 2001, *ApJ*, 551, 394
- Minami S., Ota N., Yamauchi S., Koyama K., 2013, *PASJ*, 65
- Misanovic Z., Kargaltsev O., Pavlov G. G., 2010, *ApJ*, 725, 931
- Moffett D., Gaensler B., Green A., Slane P., Harrus I., Dodson R., 2002, in ASP Conf. Series 271. p. 221
- Morton T. D., Slane P., Borkowski K. J., Reynolds S. P., Helfand D. J., Gaensler B. M., Hughes J. P., 2007, *AJ*, 667, 219
- Ng C. Y., Bucciantini N., Gaensler B. M., Camilo F., Chatterjee S., Bouchard A., 2012, *ApJ*, 746, 1
- Nugent J. J., Pravdo S. H., Garmire G. P., Becker R. H., Tuohy I. R., Winkler P. F., 1984, *ApJ*, 284, 612
- Nynka M., et al., 2013, *ApJ Letters*, 778, 1
- Odegard N., 1986, *ApJ*, 301, 813
- Pannuti T. G., Rho J., Borkowski K. J., Cameron P. B., 2010, *AJ*, 140, 1787
- Pannuti T. G., Rho J., Heinke C. O., Moffitt W. P., 2014a, *AJ*, 147, 55
- Pannuti T. G., Kargaltsev O., Napier J. P., Brehm D., 2014b, *ApJ*, 782
- Park G., et al., 2013, *ApJ*, 777, 14
- Petriella A., Paron S. A., Giacani E. B., 2013, *A&A*, 554, A73
- Phillips J. P., Marquez-Lugo R. A., 2010, *MNRAS*, 409, 701
- Pihlström Y. M., Sjouwerman L. O., Frail D. A., Claussen M. J., Mesler R. A., McEwen B. C., 2014, *AJ*, 147
- Pye J. P., Becker R. H., Seward F. D., Thomas N., 1984, *MNRAS*, 207, 649
- Rakowski C. E., Hughes J. P., Slane P. O., 2001, *ApJ*, 548, 258
- Rakowski C. E., Badenes C., Gaensler B. M., Gelfand J. D., Hughes J. P., Slane P. O., 2006, *ApJ*, 646, 982
- Ranasinghe S., Leahy D. A., 2018, *AJ*, 155, 204
- Reach W. T., et al., 2006, *AJ*, 131, 1479
- Reich W., Furst E., Sofue Y., 1984, *A&A*, 133, L4
- Reich W., Zhang X., Furst E., 2003, *A&A*, 408, 961
- Reynolds S. P., 2006, *ApJ*, 652, L45
- Reynolds M. T., et al., 2013, *ApJ*, 766, 112
- Reynoso E. M., Mangum J. G., 2000, *ApJ*, 20, 874
- Reynoso E. M., Johnston S., Green A. J., Koribalski B. S., 2006, *MNRAS*, 369, 416
- Rho J., Borkowski K. J., 2002, *ApJ*, 575, 44
- Roy S., Pal S., 2013, *PIAU*, 9, 197
- Sabin L., et al., 2013, *MNRAS*, 431, 279
- Sarma A., Goss W., Green A., Frail D. A., 1997, *ApJ*, 483, 335
- Sasaki M., Plucinsky P. P., Gaetz T. J., Bocchino F., 2013, *A&A*, 552, A45
- Sato F., 1979, *ApL*, 20, 43
- Sato T., Koyama K., Lee S. H., Takahashi T., 2016, *PASJ*, 68, S81
- Sezer A., Gök F., 2014, *ApJ*, 790, 5
- Shan S. S., Zhu H., Tian W. W., Zhang M. F., Zhang H. Y., Wu D., Yang A. Y., 2018, *ApJS*, 238, 35
- Slane P., et al., 2012, *ApJ*, 749, 131
- Smith A., Jones L. R., Peacock A., Pye J. P., 1985, *ApJ*, 296, 469
- Surnis M. P., Joshi B. C., Maan Y., Krishnakumar M. A., Manoharan P. K., Naidu A., 2016, *ApJ*, 826, 184
- Takata A., Nobukawa M., Uchida H., Tsuru T. G., Tanaka T., Koyama K., 2016, *PASJ*, 68, S31
- Tian W. W., Leahy D. A., 2006, *A&A*, 455, 1053
- Tian W. W., Leahy D. A., 2008, *MNRAS*, 58, 54
- Tian W. W., Leahy D. A., 2012, *MNRAS*, 421, 2593
- Tian W. W., Leahy D. A., 2014, *ApJ*, 783, L2
- Tian W. W., Havercorn M., Zhang H. Y., 2007a, *MNRAS*, 378, 1283
- Tian W. W., Li Z., Leahy D. A., Wang Q. D., 2007b, *ApJ*, 657, L25
- Tian W. W., Leahy D. A., Li D., 2010, Distance to the SNR CTB 109/AXP 1E 2259+586 by HI absorption and self-absorption ([arXiv:1002.1093](https://arxiv.org/abs/1002.1093)), doi:[10.1111/j.1745-3933.2010.00822.x](https://doi.org/10.1111/j.1745-3933.2010.00822.x)
- Torii K., Uchida H., Hasuike K., Tsunemi H., Yamaguchi Y., Shibata S., 2006, *PASJ*, 58, 11
- Tsuji N., Uchiyama Y., 2014, *PASJ*
- Uyaniker B., Kothes R., Brunt C., 2002, *ApJ*, 565, 1022
- Vink J., 2004, *ApJ*, 604, 7
- Voisin F., Rowell G., Burton M. G., Walsh A., Fukui Y., Aharonian F., 2016, *MNRAS*
- Whiteoak J. B. Z., 1992, *MNRAS*, 256, 121
- Wolszczan A., Cordes J. M., Dewey R. J., 1991, *ApJ*, 372, L99
- Xu J. L., Wang J. J., 2012, *A&A*, 543, A24
- Yamaguchi H., Ueno M., Koyama K., Bamba A., Yamauchi S., 2004, *PASJ*, 56, 1059
- Yamaguchi H., Tanaka M., Maeda K., Slane P. O., Foster A., Smith R. K., Katsuda S., Yoshii R., 2012, *ApJ*, 749, 137
- Yamaguchi H., et al., 2015, *ApJ*, 801, L31
- Yamauchi S., Minami S., Ota N., Koyama K., 2014, *ASJ*, 66, 1
- Yar-Uyaniker A., Uyaniker B., Kothes R., 2004, *ApJ*, 616, 247

- Yasumi M., Nobukawa M., Nakashima S., Uchida H., Sugawara R., Tsuru T. G., Tanaka T., Koyama K., 2014, [PASJ](#), 66, 1
Zhang G. Y., Chen Y., Su Y., Zhou X., Pannuti T. G., Zhou P., 2015, [ApJ](#), 799
Zhao J. H., Morris M. R., Goss W. M., 2013, [ApJ](#), 777, 1
Zhou P., Chen Y., 2011, [ApJ](#), 743, 4
Zhou P., Chen Y., Safi-Harb S., Zhou X., Sun M., Zhang Z.-Y., Zhang G.-y., 2016, [ApJ](#), 831
Zhu H., Tian W. W., Torres D. F., Pedaletti G., Su H. Q., 2013, [ApJ](#), 775, 95
Zhu H., Tian W. W., Zuo P., 2014, [ApJ](#), 793
Zoglauer A., et al., 2015, [ApJ](#), 798, 4

This paper has been typeset from a [TeX/LaTeX](#) file prepared by the author.